AIChE

Draw Ratio Enhancement in Nonisothermal Melt Spinning

Balram Suman and Satish Kumar
Dept. of Chemical Engineering and Materials Science, University of Minnesota, Minneapolis, MN 55455

DOI 10.1002/aic.11707
Published online February 4, 2009 in Wiley InterScience (www.interscience.wiley.com).

Nonisothermal melt spinning of materials having a step-like viscosity variation with temperature is studied in this work. A set of nonlinear equations is used to describe the fiber behavior and to obtain the draw ratio, the square of the ratio of the fiber diameter at the entrance to that at the exit of the fiber-spinning device. The fluid-flow equation is based on a slender-jet approximation, and external heating and cooling have been accounted for with a one-dimensional model in order to obtain the fiber temperature and viscosity along the fiber length. The model is similar to that used by Wylie et al. (J Fluid Mech. 2007;570:1–16) but accounts for inertia, shear stress at the fiber surface, surface tension, gravity, cooling, and larger heating rates. Steady-state analysis reveals that the draw ratio increases with an increase in the pulling force, passes through a maximum, and then starts increasing again, resulting in three possible pulling forces for the same draw ratio. However, linear stability analysis reveals that depending on the strength of heating and/or cooling, at most two of the steady states are stable. The stability analysis also predicts complicated oscillatory and nonoscillatory dynamical behavior as the pulling force varies. Nonlinear simulations reveal that an unstable system always tends to limit-cycle behavior. Systems predicted as stable by the linear stability analysis are also stable for large-amplitude perturbations. External heating is found to dramatically enhance the draw ratio of the melt-spinning process. The addition of a cooling section suppresses the draw ratio, but this can be compensated for with a higher heating strength. © 2009 American Institute of Chemical Engineers *AIChE J,* 55: 581–593, 2009

Keywords: Polymer processing, mathematical modeling, melt spinning, nanofibers

Introduction

Submicron-size fibers possess several valuable characteristics such as large surface-to-volume ratio, flexibility in surface functionality, and superior mechanical performance. A mat formed by submicron-size fibers has high porosity and can filter micron-size particles (e.g., pollen spores). Such outstanding properties make these fibers suitable for a variety of potential applications such as filtration, membrane separations, protective military clothing, biosensors, wound dressing, and scaffolds for tissue engineering.[1–5] However, there is a need to improve processes for submicron-size fiber production since the currently used nanofiber production processes have a low production rate. In this work, we consider a melt-spinning (MS) process for materials possessing a step-like change in viscosity with temperature. Important classes of materials such as block copolymers and multicomponent polymer melts[6,7] have a viscosity that behaves in this way, making it essential to investigate their MS behavior. Nonisothermal MS studies have thus far largely been confined to materials showing an exponential variation of viscosity with temperature.[8–12]

Three commonly used processes to produce fibers are electrospinning (ES), melt blowing (MB), and MS. In ES, a strong electrical potential (~10 kV) is applied to a polymer solution

Correspondence concerning this article should be addressed to S. Kumar at kumar@cems.umn.edu.

in a syringe to force a jet of solution onto a grounded screen located a few centimeters away. Rapid evaporation of the solvent results in a mat of fine (10 nm to 1 μm) polymer fibers deposited onto the screen. This is currently used to produce nanofibers,[13,14] but the process is inherently slow because of the requirement of removing residual solvent from the fibers, and is undesirable because of the difficulty in solvent handling/recovery.[5,15] As a result, the process is costly. Furthermore, many polymers are hard to dissolve in common solvents at room temperature, making them difficult to electrospin. MB is performed by extruding a polymer melt and drawing it down using an air jet of high velocity at the polymer–air interface. Then, fibers are collected on a mat located a few centimeters away. This process has also recently been shown to produce nanofibers.[16] However, the fiber size distribution is not narrow, which is desired for biological applications.[17] In MS, fiber drawing is due to a take-up wheel instead of an air jet. This process is restricted to producing fibers with diameters larger than 10 μm.[1] But, MS has advantages when compared with the other two processes.[18,19] For example, its production rate is $\sim$10 and 100 times higher than MB and ES, respectively. It is also cheap, environmentally friendly, and easier to control. In addition, the fiber solidifies during the drawing process in MS, which yields oriented chains resulting in strong fibers with better size uniformity and chemical and mechanical stability.

Isothermal and nonisothermal MS operations are well documented in the literature (Refs. 8, 18, 19 and references therein). Thus, instead of presenting a detailed literature review, we note the distinguishing features of the present work. As mentioned above, important classes of materials show a step-like variation in viscosity with temperature. Fiber drawing of such materials was recently studied by Wylie et al.[7] Their study provides steady-state and linear stability analyses and focuses the occurrence of multiple steady states. Their work does not account for the effects of inertia, surface tension, shear stress at the polymer–air interface, gravity, and cooling and also does not attempt to investigate draw ratio enhancement. The draw ratio, Dr, is the square of the ratio of the fiber diameter at the entrance to that at the exit and is an important process variable. In this work, we account for all of these effects and perform steady-state and linear stability analyses, as well as nonlinear simulations to study the effect of large-amplitude disturbances. In addition, we derive a set of equations governing fiber behavior by using a slender-jet approximation, connect them with related equations presented in the literature, and investigate Dr enhancement using external heating, an effect not addressed by Wylie et al.[7] The rest of the article is organized as follows: the model for the MS process is developed in the next section. The following two sections deal with steady-state behavior and linear stability analysis. We then turn to nonlinear simulations and the effects of a cooling section before presenting a summary and conclusions.

Problem Formulation

In a MS process, molten polymer (polymer filament) comes out from a die. The attenuation in the diameter of the polymer filament is achieved using an external force applied by a take-up roller. Sometimes external air is used to cool the polymer filament. In this work, we suppose that an external heater along the length of the polymer filament acts to decrease the polymer viscosity. The schematic of the process is presented in Figure 1. The momentum and mass conservation equations are

$$\rho(\partial_t \mathbf{u} + \mathbf{u}\cdot\nabla\mathbf{u}) = -\nabla p + \nabla\cdot\tau + \rho g\mathbf{e}_z, \tag{1}$$

$$\nabla\cdot\mathbf{u} = 0, \tag{2}$$

where $\mathbf{u} = (u_r,u_\theta,u_z) = (w,0,u)$ is the velocity, p is the pressure, and $\tau = \mu(\nabla\mathbf{u} + (\nabla\mathbf{u})^*)$ is the extra-stress tensor for an incompressible Newtonian fluid with the superscript "*" denoting transpose and μ denoting the dimensional viscosity of the molten polymer filament. Also, ρ is the density, g is the gravitational acceleration, ∂_t is the time derivative, and $\mathbf{e}_z$ is the unit vector in the z-direction. The energy conservation equation is:

$$\rho C_p(\partial_t T + \mathbf{u}\cdot\nabla T) = -\nabla\cdot\mathbf{q}, \tag{3}$$

where C_p is the heat capacity, T is the temperature, and $\mathbf{q}$ is the heat flux at the fiber-air interface. At this interface, the stress balance is:

$$\pi\cdot\mathbf{n} = -\kappa\sigma\mathbf{n} + S\mathbf{t}, \tag{4}$$

where π is the total-stress tensor, σ is the surface tension, κ is twice the mean curvature, $\mathbf{n}$ is the outward unit normal vector, $\mathbf{t}$ is the unit tangential vector, and S is the external shear stress at the interface due to imposed air flow. A kinematic boundary condition is also needed:

$$w|_{r=h^*} = \partial_t h^* + u\partial_z h^*, \tag{5}$$

where h^* is the location of the fiber-air interface, and ∂_z denotes differentiation with respect to z. Finally, for a boundary condition involving energy, we use:

$$\mathbf{q}\cdot\mathbf{n} = f(z), \tag{6}$$

where $f(z)$ is the heat flux supplied by the heater.

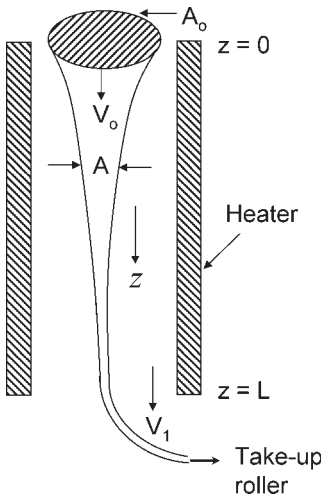

Figure 1. Schematic of a MS process with external heating.

The following assumptions have been made in deriving the final set of equations: (i) the fiber is like a slender jet; (ii) incompressible fiber material; (iii) negligible die swell; (iv) neglect of heat conduction in the fiber; and (v) constant density, heat capacity, and surface tension for the fiber. All of these assumptions have been shown to be valid for the conditions of industrial MS except negligible die swell,[18,19] which could lead the model to predict smaller fiber diameters. This may be accounted for by considering a slightly larger diameter for the polymer filament at the die exit.[19]

We scale length in the z-direction with L, length in the r-direction with r_o, time with L/V_o, and velocity in the z- and r-directions with V_o and r_oV_o/L, respectively, where L is the length of the domain for the fiber attenuation, r_o is the radius of the fiber at $z = 0$, and V_o is the velocity in the z-direction at $z = 0$. Pressure is scaled by ρV_o^2, and viscosity by μ_o, the viscosity at $z = 0$. We consider the limit where $\varepsilon = r_o/L \ll 1$. The dimensionless variables have been represented using the same variables as before but with a tilde over them. Then, the z-component of Eq. 1 becomes

$$\frac{\epsilon^2\rho LV_o}{\mu_o}\left(\frac{\partial\tilde{u}}{\partial\tilde{t}}+\tilde{w}\frac{\partial\tilde{u}}{\partial r}+\tilde{u}\frac{\partial\tilde{u}}{\partial\tilde{z}}\right) = -\frac{\epsilon^2\rho V_oL}{\mu_o}\frac{\partial\tilde{p}}{\partial\tilde{z}}+\frac{1}{\tilde{r}}\frac{\partial}{\partial\tilde{r}}\left(\mu\tilde{r}\frac{\partial\tilde{u}}{\partial\tilde{r}}+\epsilon^2\mu\tilde{r}\frac{\partial\tilde{w}}{\partial\tilde{z}}\right) + 2\epsilon^2\frac{\partial}{\partial\tilde{z}}\left(\mu\frac{\partial\tilde{u}}{\partial\tilde{z}}\right)+\frac{\epsilon^2\rho gL^2}{V_o\mu_o}+O(\epsilon^4), \quad (7)$$

where μ is the dimensionless viscosity at any location z. The functional form of the viscosity variation will be discussed at the end of this section. Henceforth, we drop the tilde. We now express u,w, and p as follows:

$$\begin{aligned} u &= u_o(z,t)+(\epsilon r)^2u_2(z,t)+O(\epsilon^4),\\ w &= -\partial_zu_o(z,t)\frac{r}{2}-\partial_zu_2(z,t)\frac{\epsilon^2r^3}{4}-O(\epsilon^4),\\ p &= p_o(z,t)+p_2(z,t)(\epsilon r)^2+O(\epsilon^4). \end{aligned} \quad (8)$$

The expression for w is obtained using the expression for u and Eq. 2. Then, Eq. 7 leads to

$$\frac{\rho LV_o}{\mu_o}(\partial_tu_o+u_o\partial_zu_o) = -\frac{\rho V_oL}{\mu_o}\partial_zp_o + (4\mu u_2-\mu\partial_z^2u_o+2\partial_z(\mu\partial_zu_o))+\frac{\rho gL^2}{V_o\mu_o}+O(\epsilon^2). \quad (9)$$

The normal and shear stress balances give

$$\begin{aligned} \partial_zp_o &= \frac{\sigma}{\rho r_oV_o^2}\partial_z\kappa-\frac{\mu_o\partial_z(\mu\partial_zu_o)}{\rho V_oL}+O(\epsilon^2),\\ 4\mu u_2 &= \frac{6\mu\partial_zu_o\partial_zh^*+h^*\mu\partial_z^2u_o+3S}{h^*}+O(\epsilon^2), \end{aligned} \quad (10)$$

where S is now a dimensionless shear stress, scaled by $6\mu_oV_or_o^2/L$, and h^* is the dimensional location of the fiber–air interface. The quantity $\kappa = 1/h^* + O(\varepsilon^2)$. Retaining only leading order terms and dropping the subscript "o" from u_o, Eq. 9 becomes

$$Re(\partial_tu+u\partial_zu) = \frac{C}{h^{*2}}\partial_zh^*+\left(\frac{2\mu\partial_zu\partial_zh^*}{h^*}+\partial_z(\mu\partial_zu)\right)+\frac{S}{h^*}+\frac{Re}{Fr}, \quad (11)$$

where $Re = \rho LV_o/3\mu_o$, $C = \sigma L/3\mu_oV_or_o$, and $Fr = V_o^2/gL$. Here, Re is the Reynolds number, C is the inverse capillary number, and Fr is the Froude number. The dimensionless kinematic boundary condition reduces to

$$\partial_th^*+u\partial_zh^* = -\frac{h^*}{2}\partial_zu|_{r=h^*}, \quad (12)$$

where all variables are in dimensionless form.

The above equations are equivalent to those used by previous researchers. Letting $L = v^2\rho/\sigma$, $V_o = \sigma/v\rho$, and neglecting external shear stress, gravity, and viscosity variation, we obtain $Re = 1/3$, $C = 1/3$, and $S = Re/Fr = 0$. Then, Eqs. 11 and 12 become

$$\partial_tu+u\partial_zu = \frac{\partial_zh^*}{h^{*2}}+3\left(\frac{2\partial_zu\partial_zh^*+h^*\partial_{zz}u}{h^*}\right), \quad (13)$$

$$\partial_th^*+u\partial_zh^* = -\frac{h^*}{2}\partial_zu|_{r=h^*}, \quad (14)$$

which are same as those reported in Eggers' work on breakup of liquid jets.[20] Letting $L = 9v^2\rho/\sigma$, $V_o = \sigma/3v\rho$, and imposing constant viscosity ($\mu(\theta) = 1$), we obtain $Re = 1$, $Re/Fr = 1$, and $C = 1$. Writing Eqs. 11 and 12 in terms of the cross-sectional area (A) of the fiber yields

$$\partial_tu+u\partial_zu = \frac{\partial_z\sqrt{A}}{A}+\frac{\partial_z(A\partial_zu)}{A}+1, \quad (15)$$

$$\partial_tA+\partial_z(Au) = 0. \quad (16)$$

These equations are the same as those used by Sauter and Buggisch,[21] who studied the stability of a viscous jet driven by gravity. Referring to the dimensional form of Eq. 11 and rearranging, we get

$$\rho u\partial_zu = \rho g-3\mu\frac{(\partial_zu)^2}{u}+3\mu\partial_{zz}u+3\partial_z\mu\partial_zu-\sigma\sqrt{\pi}\frac{\partial_zu}{2\sqrt{Qu}}, \quad (17)$$

where Q is the dimensional volumetric flow rate and μ is the dimensional viscosity. This equation is used in Shah and Pearson's work on modeling of a molten viscous polymer filament.[22]

We next simplify the energy conservation law, Eq. 3. When $\tilde{T} = (T - T_o)/T_c$, where T_c is the temperature increase from the fiber temperature at $z = 0$ (denoted by T_o) needed for a significant drop in viscosity, Eq. 3 becomes

$$\frac{\partial\tilde{T}}{\partial\tilde{t}}+\tilde{w}\frac{\partial\tilde{T}}{\partial\tilde{r}}+\tilde{u}\frac{\partial\tilde{T}}{\partial\tilde{z}} = \frac{kL}{\rho C_pV_o}\left(\frac{1}{\epsilon^2\tilde{r}}\frac{\partial}{\partial\tilde{r}}\left(\tilde{r}\frac{\partial\tilde{T}}{\partial\tilde{r}}\right)+\frac{\partial^2\tilde{T}}{\partial\tilde{z}^2}\right)+O(\epsilon^2), \quad (18)$$

where k is the thermal conductivity and C_p is the heat capacity of the fiber. Now, expressing $T = \theta_o(z,t) + \theta_2(z,t)(\varepsilon r)^2 + \cdots$, and dropping the tilde, we get

$$\frac{\partial \theta_o}{\partial t} + u_o \frac{\partial \theta_o}{\partial z} = \frac{k}{\rho C_p V_o L}\left(\frac{\partial^2 \theta_o}{\partial z^2} + 4\theta_2\right) + O(\epsilon^2). \quad (19)$$

The expression for θ_2 can be obtained by equating the heat flux at the fiber–air boundary; we obtain

$$\theta_2 = -\frac{r_o}{2kT_c}\frac{f(z)}{h^*} + O(\epsilon^2), \quad (20)$$

and retaining only leading order terms, the energy balance Eq. 19 leads to

$$\frac{\partial \theta_o}{\partial t} + u_o \frac{\partial \theta_o}{\partial z} = \frac{k}{\rho C_p V_o L}\frac{\partial^2 \theta_o}{\partial z^2} - \frac{2r_o}{\rho C_p L V_o T_c}\frac{f(z)}{h^*}. \quad (21)$$

We again drop the subscript "o" from now on. As the axial conduction in a polymeric filament is small ($k/\rho C_p V_o L \sim 10^{-2}$),[7] the energy equation can be approximated as

$$\partial_t \theta + u\partial_z \theta = -\frac{2r_o}{\rho C_p L V_o T_c}\frac{f(z)}{h^*}, \quad (22)$$

where $f(z) = \alpha k_B (L/r_o)^2 T_h^4 (T_h^{-4}(\theta T_c + T_o)^4 - 1)$ for radiation where k_B is the Boltzmann constant, α is the absorptivity of the fiber, T_h is the heater temperature, and θ is the fiber temperature at z. Writing Eqs. 11, 12, and 22 in terms of A, we obtain

$$A\,Re(u_t + uu_z) = \left(\mu(\theta)Au_z + C\sqrt{A}\right)_z + \frac{Re}{Fr}A + S\sqrt{A}, \quad (23)$$

$$\theta_t + u\theta_z = \frac{H}{\sqrt{A}}, \quad (24)$$

$$A_t + (Au)_z = 0, \quad (25)$$

where $H = -2\sqrt{\pi}Lf(z)/\rho C_p r_o V_o T_c$ is the dimensionless heat flux and measures the strength of heating, and the subscripts z and t denote differentiation with respect to z and t, respectively. The constant value of H assumes $T \ll T_h$. Note that $H > 0$ corresponds to heating, whereas $H < 0$ corresponds to cooling. The corresponding boundary conditions are $u = 1$, $A = 1$, and $\theta = 0$ at $z = 0$, and $u = \mathrm{Dr}$ at $z = 1$, where Dr is the square of the ratio of the diameter at $z = 0$ to that at $z = 1$, i.e., $\mathrm{Dr} = d_o^2/d_1^2 = u_1/u_o$ with d denoting the fiber diameter. We recover the model of Wylie et al.[7] when $Re = C = S = Re/Fr = 0$.

Arrhenius-type (exponential) viscosity variation with temperature has been used to model MS for polymers[8–10,22,23] and glasses.[11,12] However, important classes of materials, such as block copolymers and multicomponent polymer melts, show abrupt changes in viscosity with temperature.[6,7] Polymer crystallization is also accompanied by steep changes in viscosity.[19] Step-functions have been used to model these sharp variations in viscosity with temperature.[7,24] For computational ease, we have employed a hyperbolic tangent function similar to Wylie et al.[7] to obtain a step-like variation in the viscosity. In dimensional form, we have

$$\mu(T) = \mu_o\left[\frac{(1+M)}{2} - \frac{(1-M)}{2}\tanh\left(\frac{T - T_o - T_c}{T_r}\right)\right], \quad (26)$$

where μ is the viscosity of the fiber at any temperature T, μ_o is the viscosity at the lower temperature, $M\mu_o$ is the viscosity at higher temperature, and T_r is a characteristic temperature at which the change in viscosity occurs. Thus, M (<1) sets the amount of viscosity drop, and T_r controls the steepness of the viscosity change. As a result, this viscosity variation could also cover qualitative features of an exponential change by varying T_r. The nondimensionlized equation corresponding to Eq. 26 results in

$$\mu(\theta) = \frac{(1+M)}{2} - \frac{(1-M)}{2}\tanh[K(\theta - 1)], \quad (27)$$

where $K = T_c/T_r$ controls the steepness of the viscosity variation with temperature. For results presented in this work, $K = 12$ and $M = 0.1$ have been employed to be consistent with Wylie et al.[7]

Steady-State Behavior

We start our analysis with the investigation of steady-state behavior. A set of steady-state equations can be obtained by dropping the time-derivative terms in Eqs. 23–25. They become

$$A\,Re(uu_z) = \left(\mu(\theta)Au_z + C\sqrt{A}\right)_z + \frac{Re}{Fr}A + S\sqrt{A}, \quad (28)$$

$$u\theta_z = \frac{H}{\sqrt{A}}, \quad (29)$$

$$(Au)_z = 0, \quad (30)$$

with boundary conditions $u = 1$, $A = 1$, and $\theta = 0$ at $z = 0$, and $u = \mathrm{Dr}$ at $z = 1$.

The force required to draw the fiber is an important quantity and is called the pulling force, $F_p = |\mathbf{F}_p|$. The pulling force is obtained in a manner similar to that of Wylie et al.[7] and is given as

$$\mathbf{F}_p = \mathbf{F}_c + \mathbf{F}_s + 2\mathbf{F} + \mathbf{F}_e + \mathbf{F}_g, \quad (31)$$

where $\mathbf{F}_c$ is the force due to convection of momentum, $\mathbf{F}_s$ is the force due to surface tension, $2\mathbf{F}$ is the viscous force, $\mathbf{F}_e$ is the force due to external shear stress, and $\mathbf{F}_g$ is the force due to gravity. We can compare the typical magnitudes of these forces by considering the dimensional variables from Wylie et al.[7] and taking $\mathrm{Dr} = 100$. The quantity $F_c = \rho(Au^2)|_{z=1} = \pi\rho r_o^2\,\mathrm{Dr} \sim 10^{-5}$ N, $F_s = \pi\sigma r_o h^* = \pi\sigma r_o/\sqrt{\mathrm{Dr}} \sim 10^{-8}$N, $2F = 2\mu(Au_z)|_{z=1} = 4\pi\mu(V_o r_o^2/L)\sqrt{\mathrm{Dr}}h_z^* \sim 10^{-2}$N, $F_g \sim 10^{-6}$N, and for constant shear stress, $F_e \sim 10^{-6}S$ N. For the parameter range considered in this article, F always dominates the other forces and thus we present all results by plotting them vs. F.

In the absence of inertia, surface tension, external shear stress, and gravity ($Re = C = S = Re/Fr = 0$), $(\mu(\theta)Au_z)_z = 0$. Thus, F does not vary with z, and F_p is approximately equal to $2F$. However, when Re, C, S, and/or Re/Fr are nonzero, F varies with z, and the variation depends on the values of these parameters. However, to make the results of this study easier to compare with those of Wylie et al.,[7] we

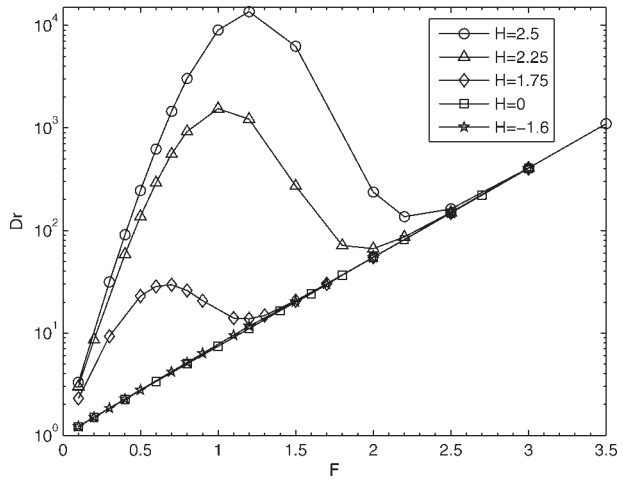

Figure 2. Dr vs. *F* for various *H* with *Re* = *C* = *S* = *Re/Fr* = 0.

consider F at $z = 0$ for presenting results, and unless stated, $Re = C = S = Re/Fr = 0$.

The coupled set of ordinary differential Eqs. 28–30 has been solved numerically with a fourth-order Runge–Kutta method to obtain Dr. In Figure 2, we present the variation of Dr with F for different H. We observe that without external heating ($H = -1.6,0$), Dr increases with increasing F. However, when external heating is applied, Dr first increases with an increase in F, passes through a maximum, and then decreases. The nonmonotonic Dr variation with F is due to viscosity variation, and thus the steady states at the lower two values of F correspond to nonisothermal operation. At high F, Dr increases with increasing F, and Dr-profiles corresponding to different heating strengths coincide; this is a regime of isothermal operation (i.e., the fiber moves so rapidly that its viscosity is almost uniform along its length). Thus, a particular Dr can be obtained at three different F (multiple steady states). Such a nonmonotonic behavior of Dr with F has been reported by Wylie et al.[7] at a low heating strength. Note that with increasing H, the maximum Dr increases, and the corresponding F shifts toward a higher value.

To investigate the multiple-steady-state behavior, we plot θ, μ, and A vs. z for three different forces corresponding to the same Dr. At low F, the velocity near $z = 0$ is small, and as a result, the time a fiber element remains in the heating zone is large. Eventually, the temperature of the fiber becomes higher than that required for the abrupt change in viscosity ($\theta > 1$). This happens at $z \sim 0.55$ and 0.8 for $F = 0.6$ and 1.49, respectively (Figure 3a). Around this position, the viscosity decreases dramatically, and after this position, the fiber has lower viscosity $\mu = M$ (Figure 3b). As F increases, the portion of the fiber having higher viscosity increases and that having lower viscosity decreases. Note that when the time is too small for a fiber element to attain the temperature required for the decrease in viscosity, the fiber viscosity remains higher ($\mu = 1$), as is the case with $F = 2.84$ in Figure 3b. Thus, adjusting the portions of the fiber having higher and lower viscosity allows the same Dr at three different forces to be attained, as shown in Figure 3c. We observe that for smaller F, the slope of the A vs. z-curve changes. The two different slopes correspond to two different viscosity values with the lower slope corresponding to the higher viscosity and the higher slope to the lower viscosity.

Analysis of the cause for the multiple steady states reveals that the steep change in the viscosity with position is the key reason for this behavior. In the present problem, it is obtained by a step-like change in viscosity governed by K

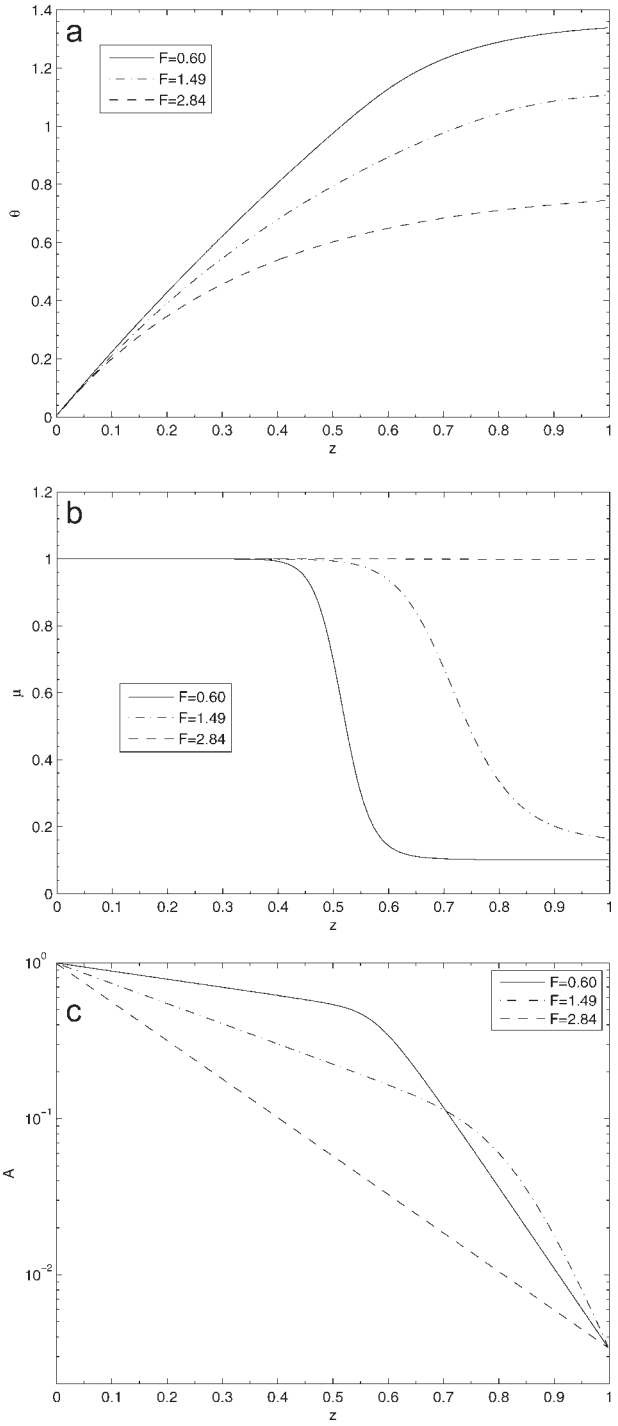

Figure 3. (a) θ vs. z, (b) μ vs. z, and (c) A vs. z for three different values of F that produce Dr $\sim$ 292.

Here, $H = 2.25$ and $Re = C = S = Re/Fr = 0$.

and M. The values $K = 12$ and $M = 0.1$ are such that we obtain multiple steady states. It is found that sufficient steepness in the viscosity variation with position is required at any heating rate to produce multiple steady states (see also Ref. 7). Note that if the viscosity does not vary steeply with temperature, multiple steady state behavior could occur provided the temperature gradient is large, perhaps because of concentrated heating.[7] It may be anticipated that steady states in the region where Dr decreases as F increases are unstable. In this region, the viscosity of the fiber drops sharply near the heater exit (Figure 3b). An increase in F would tend to reduce the amount of time the fiber spends in the heating zone, resulting in a higher viscosity at the heater exit. This would then further increase F, and eventually drive the system to a steady state at higher F corresponding to isothermal operation. Similarly, if F decreases, the time the fiber spends in the heating zone increases, resulting in a lower viscosity at the heater exit. This would further decrease F and eventually drive the system to a steady state at lower F corresponding to nonisothermal operation.

Next we study the effect of domain length by defining a parameter $l_f = L_d/L$, where L_d is the domain length. (Note that all other results are for $L_d = L$.) For a given amount of heat input, the heat flux, H_{L_d}, is calculated as $H_{L_d} = H/l_f$ where H is the heat flux value for $L_d = L$. Thus, varying l_f results in a variation in heat flux, and the longer the domain length, the lower the heat flux (for $H > 0$). The variation of Dr with l_f is presented in Figure 4. When l_f is small ($<\sim 1.5$), the heat flux is large enough to reduce the viscosity, and the portion of fiber having lower viscosity increases with l_f. Thus, Dr increases as l_f increases. However, when l_f becomes large ($\sim>2$), H decreases significantly, and this results in a lowering of the portion of fiber with lower viscosity, causing Dr to decrease as l_f increases. When l_f is very large (>3), H is not large enough to reduce the viscosity, but Dr increases with l_f, since longer domain lengths lead to higher Dr in an isothermal MS operation. Thus, multiple steady states can be obtained by varying the domain length, similar to the case where F is varied. This is again done by adjusting the portions of the fiber having higher and lower viscosity.

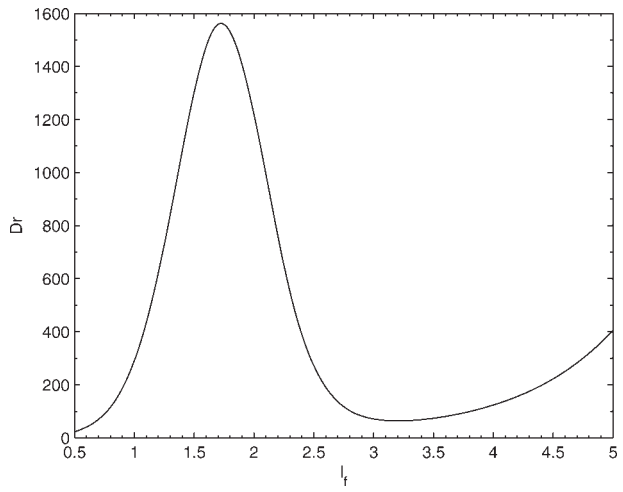

Figure 4. Variation of Dr with $l_f = L_d/L$ when $H = 2.25$, $F = 0.6$, and $Re = C = S = Re/Fr = 0$.

We have also investigated the effects of changing the cross-sectional area of the die, A_o, and found that Dr decreases as A_o increases (results not shown).

We now study the effects of Re, C, and S on the Dr variation. With nonzero Re, C, and S, F varies with z. Thus, Dr has been plotted with F at $z = 0$, denoted as F_o, in Figure 5. It is seen in Figures 5a,b that Dr increases with an increase in Re and S, respectively. This is because of higher F_p with higher Re and S. When S increases, the Dr-profile shifts toward lower F_o. Note that with $S = 1$, the region at low F_o, where Dr increases as F_o increases, vanishes. Additional calculations show that upon further increase in S, the region where Dr decreases as F_o increases also goes away, and Dr always increases with increasing F_o, corresponding to an isothermal operation. It can also be observed that increasing the value of S will lead to a decrease in the ocurrence of multiple-steady-state behavior. The effects of gravity (nonzero Re/Fr) on Dr are qualitatively the same as those of S so we do not show results here.

To account for surface tension effects, we have varied the inverse capillary number, C, and the Dr variation with F_o for various C is presented in Figure 5c. It is seen that Dr decreases with an increase in C because surface tension opposes the formation of smaller fiber diameters. At large C, the multiple-steady-state behavior of Dr is nearly suppressed, but can be made more prominent by increasing the heating strength.

Linear Stability Analysis

Three different forces can produce the same Dr, making it important to investigate the stability of these three steady states. For stability analysis, we express each variable as a sum of a steady-state term and a small-amplitude perturbation term:

$$\begin{aligned} A(z,t) &= \hat{A}(z) + \tilde{A}(z)\exp(\lambda t), \\ u(z,t) &= \hat{u}(z) + \tilde{u}(z)\exp(\lambda t), \\ \theta(z,t) &= \hat{\theta}(z) + \tilde{\theta}(z)\exp(\lambda t), \end{aligned} \tag{32}$$

where hats and tildes denote steady-state and perturbation quantities, respectively, and λ is the growth rate of the perturbation. After substitution of eq. 32 into eqs. 23–25, and linearization, a set of equations in the form of an eigenvalue problem results:

$$\lambda\tilde{A} + \left(\hat{u}\tilde{A} + \tilde{u}\hat{A}\right)_z = 0, \tag{33}$$

$$\begin{aligned} Re\left(\lambda\tilde{u}\hat{A} + \hat{A}\hat{u}_z\tilde{u} + \hat{u}\tilde{u}_z\hat{A} + \tilde{A}\hat{u}\hat{u}_z\right) &= \left[\mu(\hat{\theta})\hat{A}\tilde{u}_z + \mu(\hat{\theta})\tilde{A}\hat{u}_z + \mu_\theta(\hat{\theta})\tilde{\theta}\hat{A}\hat{u}_z\right]_z \\ &\quad + \frac{Re}{Fr}\tilde{A} + \frac{S}{2\sqrt{\hat{A}}}\tilde{A} + \frac{C}{\sqrt{\hat{A}}}\left(\tilde{A}_z - \frac{\hat{A}_z}{2\hat{A}}\tilde{A}\right), \end{aligned} \tag{34}$$

$$\lambda\tilde{\theta} + \hat{u}\tilde{\theta}_z + \tilde{u}\hat{\theta}_z + \frac{H}{2\hat{A}^{3/2}}\tilde{A} = 0, \tag{35}$$

where μ_θ is the derivative of μ with respect to θ. The boundary conditions are: $\tilde{u} = 1$ and $\tilde{\theta} = 0$ at $z = 0$, and $\tilde{u} = 0$ at $z = 1$. This eigenvalue problem has been solved numerically

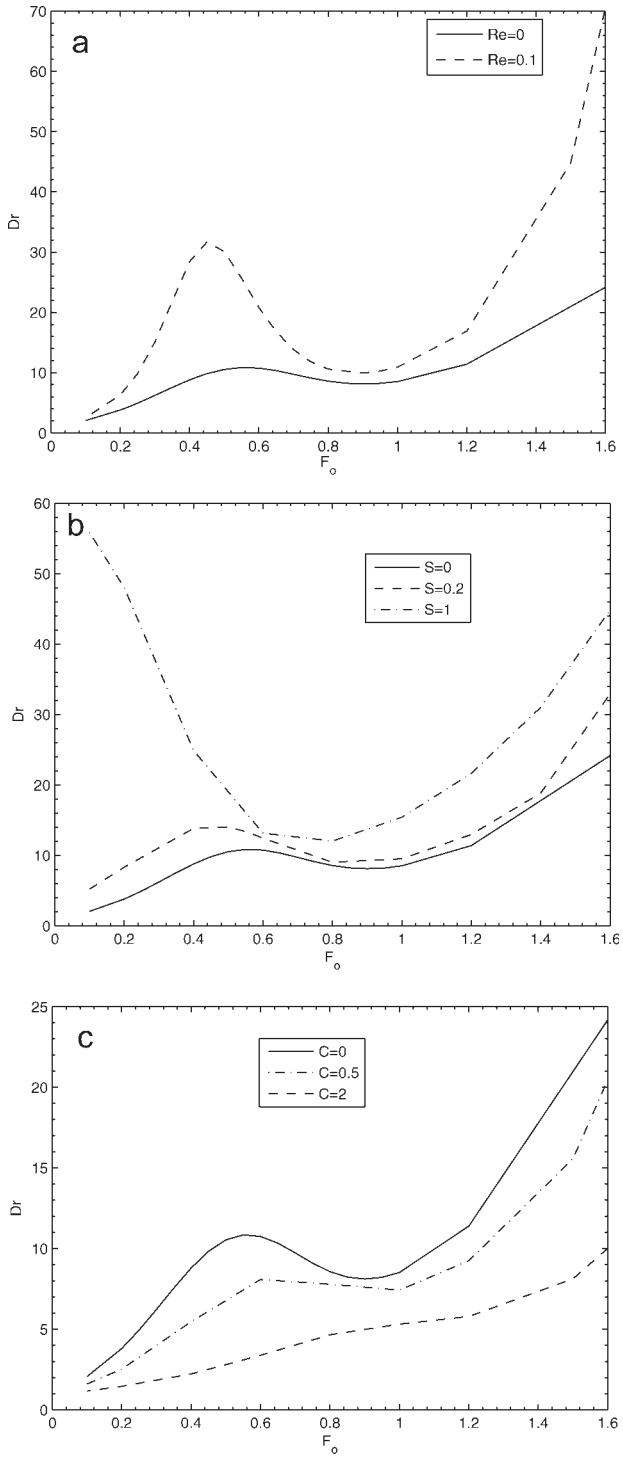

Figure 5. (a) Dr vs. F_o for various *Re* and $C = S = Re/Fr = 0$; (b) Dr vs. F_o for various *S* and $C = Re/Fr = 0$; and (c) Dr vs. F_o for various *C* and $S = Re/Fr = 0$ when $I_f = 1$ and $H = 1.6$.

in MATLAB by discretizing the equation using backward differences to approximate spatial derivatives. The results are independent of the number of nodes and the numerical method. (A forward-difference technique has also been used to verify the results.) In addition, the results obtained for $Re = C = S = Re/Fr = 0$ are in quantitative agreement with those reported in Wylie et al.[7]

To analyze the stability behavior, the real parts of the two leading eigenvalues (largest and next largest) have been plotted for different H in Figure 6. In the absence of heating, $H = 0$, the two leading eigenvalues are complex conjugates, and thus the real parts of the eigenvalues coincide (Figure 6a). The real parts of the eigenvalues increase with F, and eventually at $F \sim 1.5$ (Dr $\sim$ 20.2), they become positive (Figure 6a). This instability is called draw resonance and has been well investigated in the literature.[9,25–28] By manipulating the mass balance equation, one can obtain a kinematic wave equation in which the wave propagates from the spinneret to the take-up roller. When the wave residence time is larger than the fluid residence time, the disturbances are damped out. However, when the fluid residence time is enough to establish steady propagation of the kinematic wave, draw resonance is observed.[25,26,28] Thus, any Dr higher than $\sim$20.2 produces a fiber area that varies in an oscillatory manner with z and t. We denote this draw resonance as $I_{DR\text{-}H}$. Note that when $H = 0$, the fiber has a constant viscosity equal to the maximum value ($\mu = 1$).

When we start heating with a low heating strength, $H = 1.4$, an instability develops before $I_{DR\text{-}H}$ with complex conjugate leading eigenvalues, and the system restabilizes between this instability and $I_{DR\text{-}H}$ (Figure 6b). Kinematic wave analysis for draw resonance[28] suggests that the system should be stable in the regime where this new instability occurs (Suman B. Ph.D. Thesis, University of Minnesota, 2008). However, a plot of μ vs. z for the F corresponding to this instability reveals that there is an abrupt change in viscosity near the heater exit. Thus, it is expected that the instability is due to the change in viscosity and so we denote the instability by I_{VC}. This situation corresponds to the region where Dr decreases as F increases (cf. Figure 2), and a qualitative explanation for the instability was given earlier.

Upon further increasing the heating to $H = 1.6$, the system again goes through I_{VC}, and then restablizes before $I_{DR\text{-}H}$ (Figure 6c). When the system goes through I_{VC} at low F, it has complex conjugate leading eigenvalues. The eigenvalue with the largest real part becomes purely real, and the eigenvalue with the next-largest real part is still complex; these leading eigenvalues have different real parts (Figure 6c). Upon further increase in F, the leading eigenvalues again become complex conjugates and remain so in the range of F explored in this study.

When H is increased even further to $H = 2.25$, the nature of the stability curves remains the same as that for $H = 1.6$. However, the restabilization zone between I_{VC} and $I_{DR\text{-}H}$ diminishes resulting in a merging of I_{VC} and $I_{DR\text{-}H}$ (Figure 6d). The work of Wylie et al.[7] explored values of H up until the merging of I_{VC} and $I_{DR\text{-}H}$.

At higher heating strength, $H = 3$, the nature of the stability curves at high F remains the same as that for $H = 2.25$. However, we find an instability at lower force, $F \sim 0.3$ to 0.9, with two complex conjugate leading eigenvalues (Figure 6e), and this instability is denoted by $I_{DR\text{-}L}$. The system restabilizes between $I_{DR\text{-}L}$ and I_{VC} (Figure 6f). The instability, $I_{DR\text{-}L}$, has not been reported by Wylie et al.[7] Upon performing the kinematic wave analysis of draw resonance for

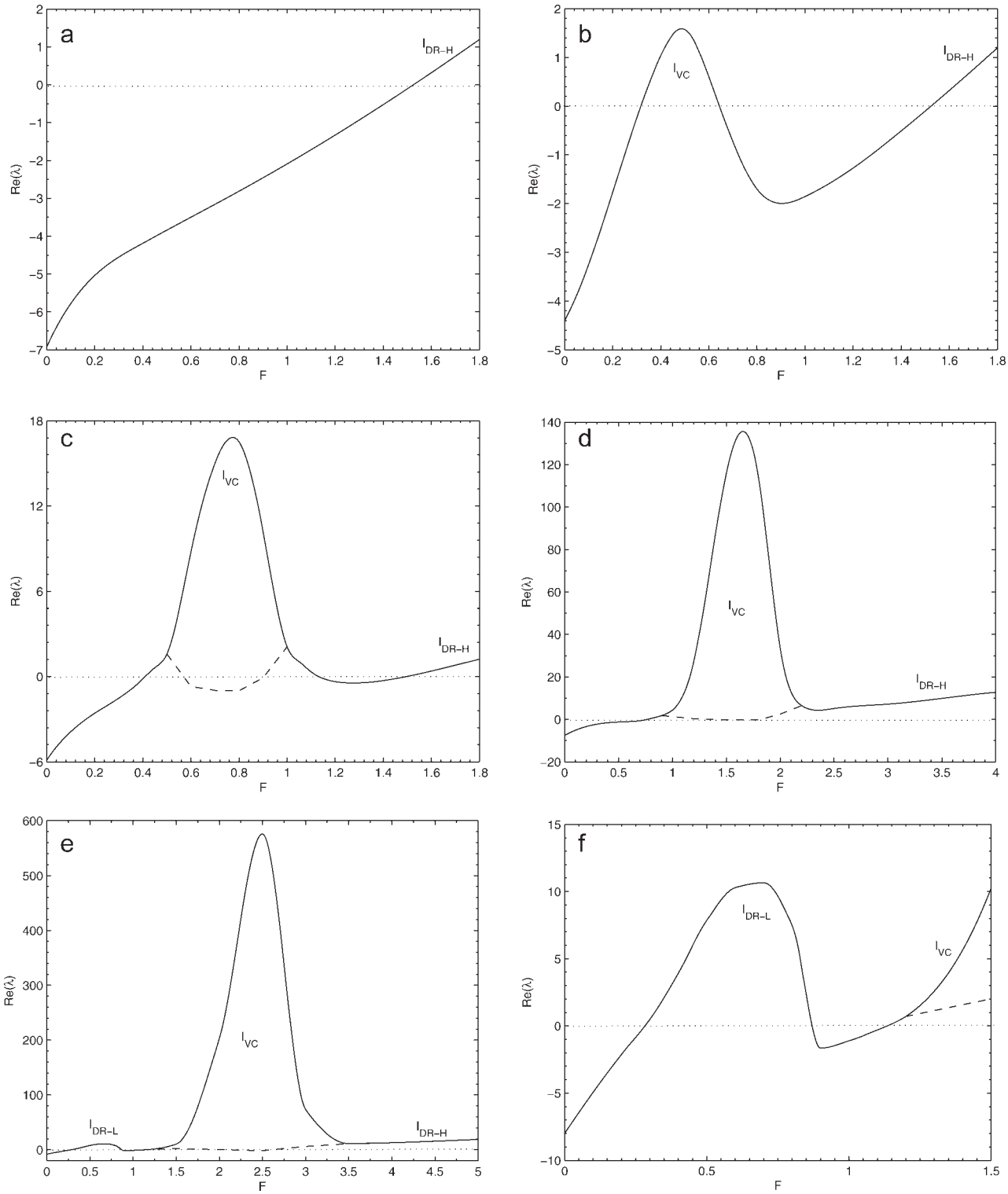

Figure 6. Plot of $Re(\lambda)$ of the two leading eigenvalues vs. F for (a) $H = 0$, (b) $H = 1.4$, (c) $H = 1.6$, (d) $H = 2.25$, (e) $H = 3$, and (f) $H = 3$, showing only the low F regime when $I_f = 1$ and $Re = C = S = Re/Fr = 0$.

the portion of fiber with lower viscosity,[28] we find that this instability is in fact draw resonance in the portion of the fiber having lower viscosity ($\mu = M$) (Suman B. Ph.D. Thesis, University of Minnesota, 2008). Note that with lower heating strength, $I_{DR\text{-}L}$ is not present since the portion of the fiber with lower viscosity is small.

The above plots show that in a nonisothermal MS process with a step-like change in viscosity, we can have three

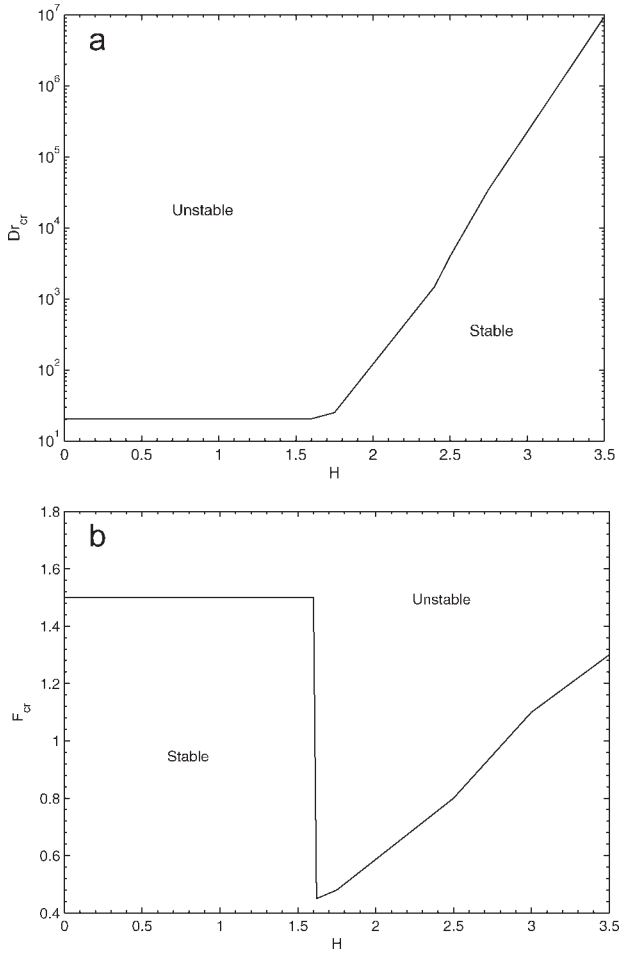

Figure 7. Dr_{cr} and F_{cr} vs. H when $l_f = 1$ and $Re = C = S = Re/Fr = 0$.

Note that in the regions marked stable, there may be pockets of instability as shown in Figure 6.

regimes of instability, $I_{DR\text{-}H}$, $I_{DR\text{-}L}$, and I_{VC}. Note that although external heating gives rise to a new instability (I_{VC}), we find that the highest Dr corresponding to a stable operation is much larger compared to that for an isothermal operation. The highest stable Dr is termed the critical Dr, denoted by Dr_{cr}, and the corresponding force is the critical F, denoted by F_{cr}.

A careful comparison of Figures 2 and 6 reveals that at low heating strength, there are at most two stable steady states for a given Dr. One stable steady state corresponds to the stable regime of the curves in Figure 6 at low F, and the other stable steady state corresponds to the restablizing zone between I_{VC} and $I_{DR\text{-}H}$. The third steady state, which is unstable, is associated with I_{VC} and occurs in the region where Dr decreases as F increases. As the heating strength is increased, the restabilizing zone between I_{VC} and $I_{DR\text{-}H}$ disappears, causing one of the stable steady states to become unstable. Thus, at high H there is at most one stable steady state. (Note that if Dr is too large at any H, there are no stable steady states.)

In Figure 7, we present Dr_{cr} and F_{cr} vs. heating strength, H. At very low H, the heating strength is not large enough to reduce the viscosity, resulting in an isothermal MS operation. Thus, Dr_{cr} and F_{cr} do not vary with H, and $F_{cr} \sim 1.5$ ($Dr_{cr} \sim 20.2$) is set by $I_{DR\text{-}H}$. When H is large enough to reduce the viscosity, but the portion of the fiber having low viscosity is small, F_{cr} is again governed by $I_{DR\text{-}H}$ (Figure 6b, and c), providing H-invariant $F_{cr} \sim 1.5$ and $Dr_{cr} \sim 20.2$ (Figure 7). As we increase H even further, F_{cr} is then governed by I_{VC} (Figure 6d) and also the portion of the fiber having low viscosity is relatively large, resulting in an exponential increase in Dr_{cr} with H (Figure 7a). However, the portion of the fiber having low viscosity is not large enough to generate $I_{DR\text{-}L}$. Note that there is a substantial reduction in F_{cr} (Figure 7b) when F_{cr} is first governed by I_{VC} instead of $I_{DR\text{-}H}$. However, F_{cr} then starts increasing with an increase in H because I_{VC} moves to higher F with increasing H (Figure 6b–e). At very high H, the portion of the fiber with lower viscosity is enough to generate $I_{DR\text{-}L}$ at low F, but because of the restabilization zone between $I_{DR\text{-}L}$ and I_{VC}, F_{cr} is still governed by I_{VC} (Figure 6f), again providing exponential enhancement in Dr_{cr} with H (Figure 7a). The exponential growth of Dr_{cr} is well approximated by $Dr_{cr} \sim \exp(3.2H)$. (The origin of the exponent, 3.2, remains unclear.) From these results, we conclude that employing external heating in MS could be used to enhance Dr_{cr} for materials showing a step-like change in viscosity. A simple calculation reveals that MS can produce submicron-size fibers. For example, if the diameter at the die exit is 0.1 mm and $Dr \sim 10^6$, the diameter of the fiber at the exit of the MS device would be $\sim 0.1\ \mu$m (100 nm).

The effects of domain length on the stability behavior have been examined by plotting the real parts of the two leading eigenvalues vs. l_f in Figure 8. At low l_f, the system is stable, but as l_f increases, the system becomes unstable, resembling Figure 6d where F is varied instead of l_f. Although the stability curves in Figure 8 are for $H = 2.25$, we have also examined other values of H and found the behavior of the stability curves to be similar to that seen in Figure 6. Thus, at a particular H, there is an optimal domain length to maximize Dr_{cr}, similar to the existence of an F_{cr} in Figure 6. For example, the optimal domain length corresponds to $l_f \sim 1.25$ when $H = 2.25$ (Figure 8). When the cross-sectional area of the die (A_o) increases, the real parts of

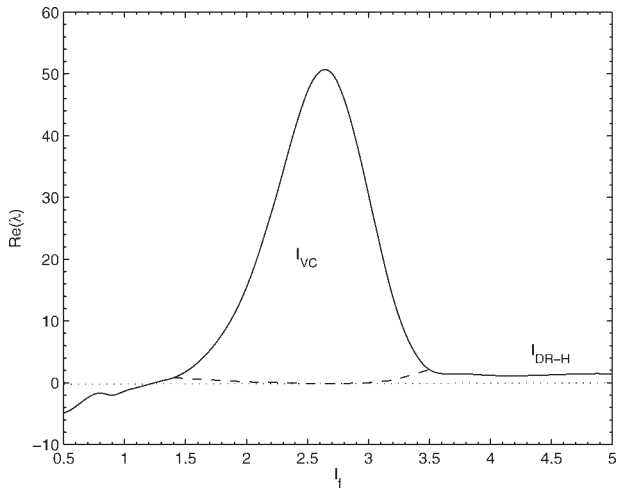

Figure 8. Plot of $Re(\lambda)$ of the two leading eigenvalues vs. l_f when $H = 2.25$, $F = 0.6$, and $Re = C = S = Re/Fr = 0$.

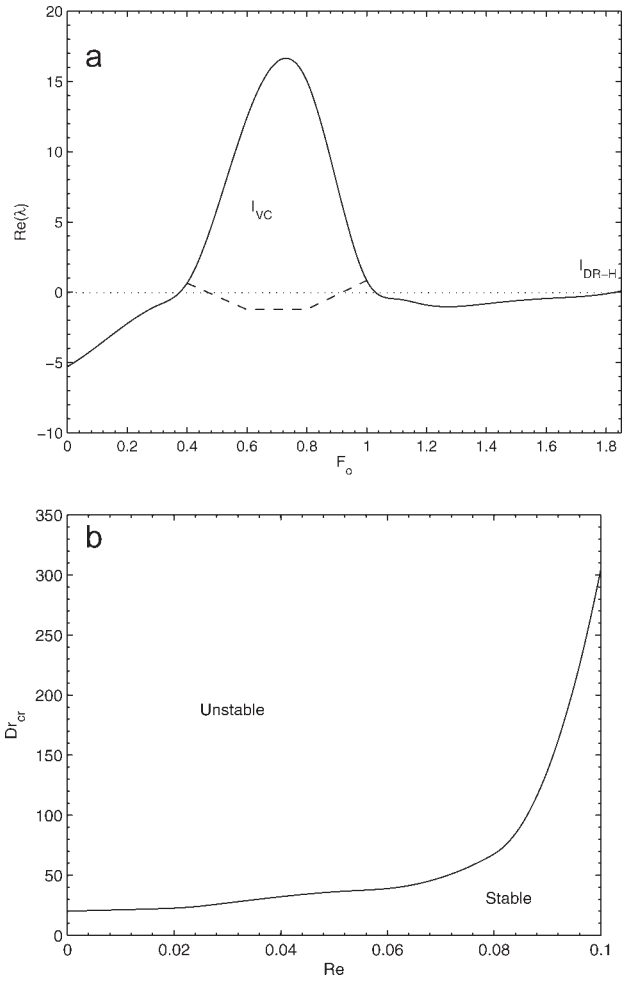

Figure 9. (a) Plot of *Re*(λ) of the two leading eigenvalues vs. *F* for *H* = 1.6 when *Re* = 0.1, I_f = 1, and *C* = *S* = 0; (b) Dr_{cr} vs. *Re*.

the leading eigenvalues also increase, suggesting that the system comes closer to instability as A_o increases (results not shown).

Next we investigate the effects of *Re, C*, and *S* on the fiber stability by comparing our results with those in with Figure 6c where $H = 1.6$ and $Re = C = S = Re/Fr = 0$. We present the leading eigenvalues when $Re = 0.1$, $C = S = 0$, and $H = 1.6$ in Figure 9a. The comparison with Figure 6c reveals that I_{VC} is similar, and a purely real positive leading eigenvalue is also obtained. However, $I_{DR\text{-}H}$ is much suppressed, as the system is stable until $F_o \sim 1.82$ in the presence of small inertia; without inertia it becomes unstable at $F_o \sim 1.55$. From Figure 5a, we see that Dr increases with an increase in *Re*. Thus, Dr_{cr} increases with increasing *Re*. This has been documented for materials other than those showing a step-like variation in viscosity with temperature (Refs 22, 29–32 and references therein). The enhancement in Dr_{cr} with *Re* for materials showing a step-like variation in viscosity with temperature is presented in Figure 9b. It is found that for $Re < 0.08$, the increase in Dr is not significant. However, when $Re > 0.08$, the increase in Dr_{cr} is nearly exponential. At $Re \sim 0.1$, $Dr_{cr} \sim 300$. Thus, it is concluded that even with materials showing step-like change in viscosity, inertia can enhance Dr. This is because the fiber velocity is controlled by the cross-sectional area of the fiber, and inertia inhibits changes in the velocity, resulting in the suppression of fiber instability (cross-sectional area variation).

Using nonzero inverse capillary number, *C*, the effects of surface tension on stability behavior are examined, and the real parts of the leading eigenvalues are presented in Figure 10a. Comparison with Figure 6c shows that as *C* increases, I_{VC} and $I_{DR\text{-}H}$ move to higher F_o, but Dr decreases with an increase in *C* at fixed F_o (Figure 5c). Thus, increasing surface tension decreases Dr_{cr}, and a similar conclusion was obtained for an isothermal MS operation by Pearson and Shah.[22,29] Comparison of Figure 10b and Figure 10a shows that inclusion of shear stress makes the system unstable at lower F_o. However, Dr increases with an increase in *S* at fixed F_o (Figure 5b). Both of these effects lead to a decrease in Dr_{cr} as *S* increases. The effects of gravity are similar to those of *S*. Increasing *Re/Fr* makes the system more unstable and also increases the value of *Dr* at fixed F_o. However,

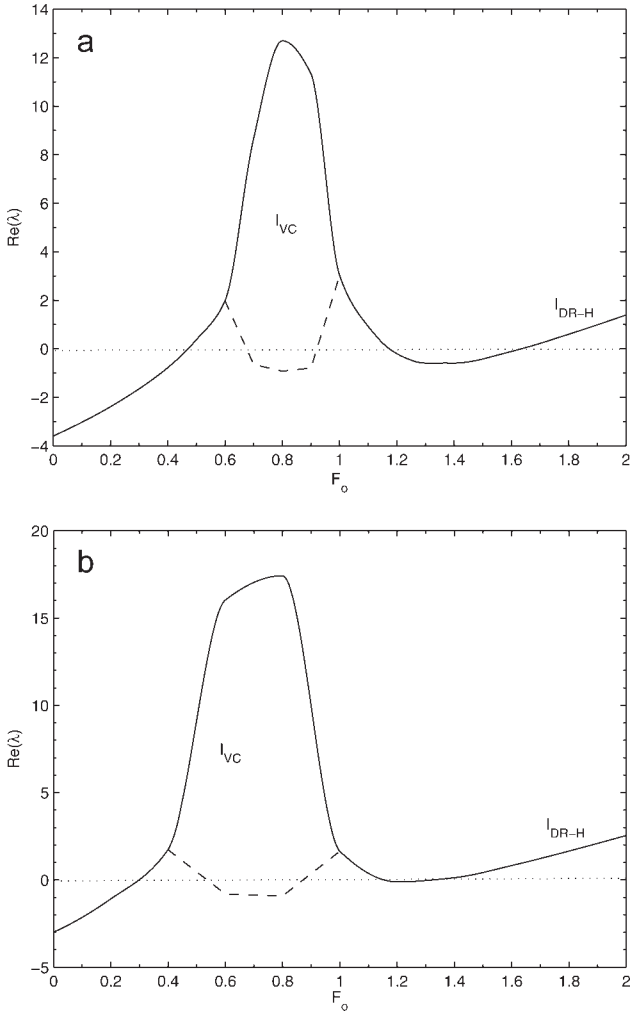

Figure 10. Plot of *Re*(λ) of the two leading eigenvalues vs. *F* when *H* = 1.6 and I_f = 1: (a) *C* = 0.5 and *Re* = *S* = 0, and (b) *S* = 0.2 and *Re* = *C* = 0.

these effects combine to produce an increase in Dr_{cr} with Re/Fr, similar to what was observed in prior work[22,29,32] for an isothermal MS operation. In all of the above cases, the changes in Dr_{cr} with respect to C, S, Re/Fr are small compared with those produced by a change in Re.

Nonlinear Simulations

To study the effects of disturbances that are not of small amplitude, we have performed nonlinear simulations using Eqs. 23–25 and the corresponding boundary conditions. The initial condition applied is a sum of a steady-state solution and a disturbance at the fiber–air interface. The disturbances are sinusoidal in nature with dimensionless amplitude varying between 0.01 and 0.5 and dimensionless wavelength varying from 0.2 to 1. These equations have been solved by discretizing the spatial derivatives using backward finite differences, and time-stepping with Gear's algorithm,[33,34] which automatically adjusts the time step. Key features of the nonlinear simulations presented in this study are independent of the amplitude and wavelength of the initial disturbances, and the number of nodes, taken as 1000.

We find that the predictions of the linear stability analysis carry over to large-amplitude disturbances. When the system is predicted stable by linear stability analysis, the initial perturbation decays with time. For an unstable system, the instability is found to be oscillatory in nature and limit cycle behavior is observed, no matter whether the instability is due to draw resonance or due to viscosity variation. Nonlinear behavior of A, u, and θ for an unstable situation is shown in Figure 11, where the cause for the instability is viscosity variation. All of these variables have been found to be oscillating with constant amplitude in time similar to the nonlinear behavior of fibers under isothermal draw resonance. Similar temporal variation of these variables has been found in other unstable cases and also with nonzero Re, C, S, and/or Re/Fr. We have shown in the steady-state analysis that the same Dr can be obtained at three F. Thus, if we start with an unstable situation and there are other stable steady states, the system jumps to one of the stable F producing same Dr.

The stabilizing effect of Re has also been probed using nonlinear simulations and it is found that by increasing inertia, an otherwise unstable system can be stabilized. We have performed nonlinear simulations for the stable and unstable regions shown in Figure 9b and observed that in the stable region, disturbances decay with time, whereas in the unstable region, disturbances grow with time and eventually they oscillate with constant amplitude similar to the behavior shown in Figure 11.

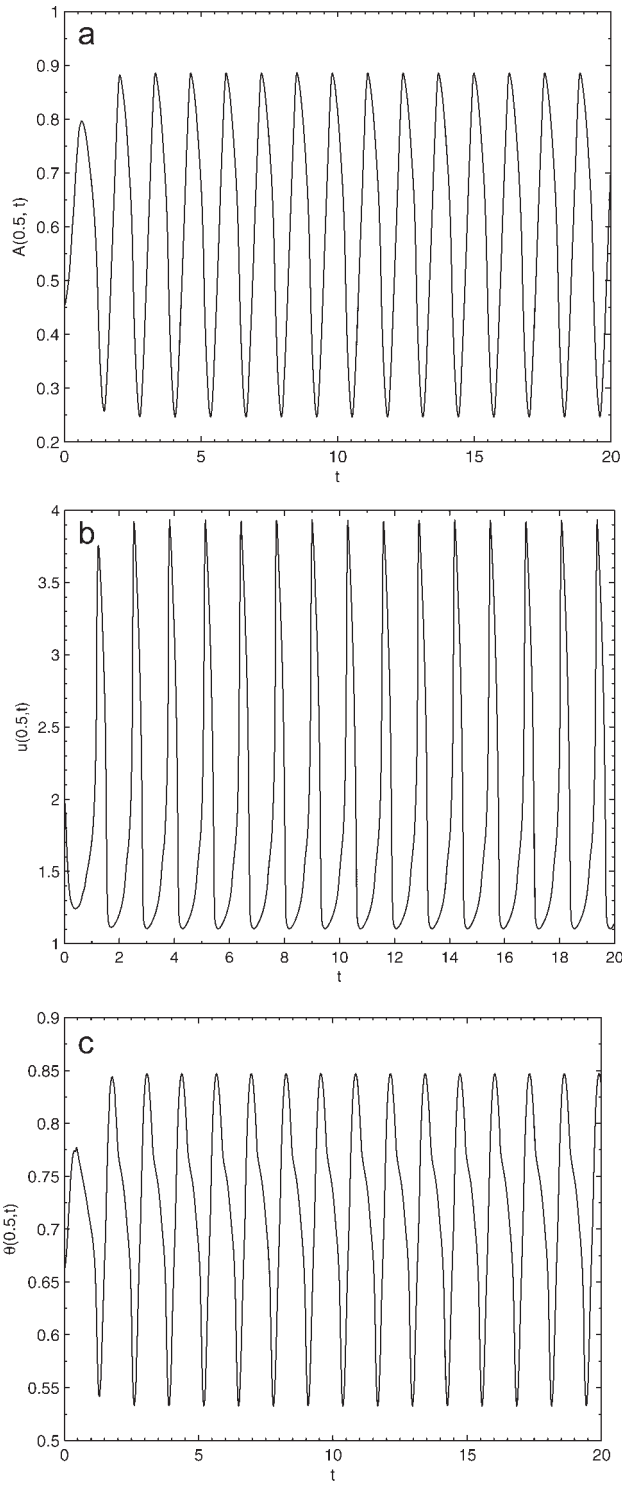

Figure 11. Nonlinear behavior when $H = 1.6$, $l_f = 1$, $F = 0.8$, and $Re = C = S = Re/Fr = 0$: (a) A, (b) u, and (c) θ.

Addition of Cooling Section

The addition of a cooling section after a heating zone could help in enhancing the viscosity of the fiber before it is taken up by a roller, which would help make rolling of fibers easier. Thus, in this section we add a cooling zone of dimensionless length l_C after a heating section of dimensionless length l_H $(= l_f - l_C)$, but before the roller. The cooling can be performed by air circulation, i.e., a convective mode of heat transfer. The fluid flow equations for the heating and cooling sections remain the same. However, the energy equation corresponding to the cooling section is different and given as:

$$\theta_t + u\theta_z = -\frac{C_o\theta}{\sqrt{A}}, \tag{36}$$

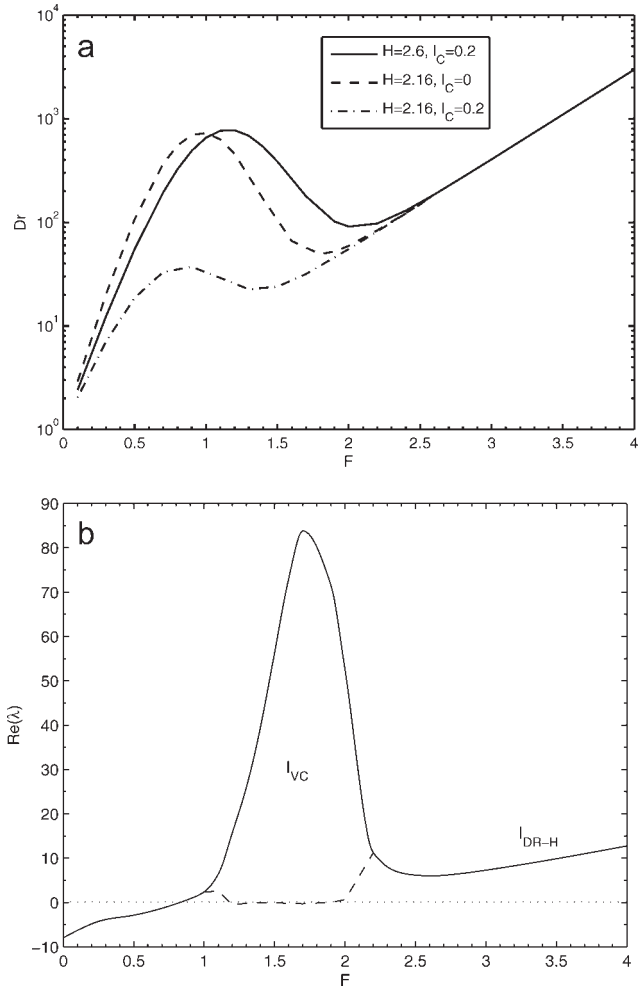

Figure 12. Effect of cooling section: (a) Dr vs. *F*, and (b) *Re*(λ) of the two leading eigenvalues vs. *F* when $H = 2.6$, $l_C = 0.2$ with $Re = C = S = Re/Fr = 0$.

The strength of cooling $C_o = -60H$ in the cooling zone is used.

where $C_o = 2\sqrt{\pi}hL/(\rho C_p V_o r_o)$ with h being a convective heat transfer coefficient and assuming $T_a \ll T_f$, where T_a represents the dimensional air temperature. The strength of cooling (C_o) is allowed to be strong enough to bring the viscosity to its original value ($\mu = 1$). The corresponding stability equation is

$$\lambda\tilde{\theta} + \hat{u}\tilde{\theta}_z + \tilde{u}\hat{\theta}_z - \frac{C_o\hat{\theta}}{2\hat{A}^{3/2}}\tilde{A} + \frac{C_o}{\hat{A}^{1/2}}\tilde{\theta} = 0. \qquad (37)$$

To investigate the cooling effect, we present the variation of Dr with F, and the real parts of the leading eigenvalues, in Figure 12. It is found that Dr decreases at a particular F when cooling is employed. This is due to an increase in the portion of the fiber having higher viscosity. However, the decrease in Dr can be compensated for by using a higher heating strength (Figure 12a), which increases the portion of the fiber having lower viscosity. Thus, the addition of a cooling section causes the system to behave as if the overall heating strength has been reduced. Similar behavior is also observed in the linear stability analysis results of Figure 12b. The stability curves for $H = 2.6$, $l_H = 0.8$, $C_o = -60H$, and $l_C = 0.2$ resemble those for the case where $H \sim 2.1$ and $l_H = l_f = 1$ (result not shown). Additional calculations reveal that these observations also carry over to the nonlinear regime. We also note that the effect of cooling on Dr variation, fiber stability and nonlinear behavior remains unchanged for a system with nonzero *Re*, *S*, *C* and/or *Re*/*Fr*.

Summary and Conclusions

We have analyzed nonisothermal melt spinning of materials having a step-like variation in viscosity with temperature. Coupled nonlinear equations governing momentum and heat transfer were derived using a slender-jet approximation and solved numerically over a large range of parameters. In the absence of heating, the draw ratio increases with an increase in the pulling force. However, with sufficiently strong external heating, the draw ratio becomes a nonmonotonic function of the pulling force and can lead to a situation where three different pulling forces are compatible with the same draw ratio. Linear stability analysis shows that two of these steady states can be stable at most. At high heating strength there are three modes of instability: two corresponding to draw resonance (in fibers having high and low viscosity) and one corresponding to the sharp change in viscosity with temperature. At lower heating strength, the latter mode is always found to be unstable. Nonlinear simulations show that an unstable system tends to limit cycle behavior, and that stable systems are stable even to large-amplitude perturbations.

Although external heating generates new instability modes, it also produces dramatic increases in the maximum stable draw ratio. Inclusion of inertia enhances this effect and also makes the system more stable. In comparison, inclusion of gravity, shear stress at the fiber–air interface, and surface tension all have a relatively small impact on the critical draw ratio. External cooling, which would be important in practice for rolling the fibers, was found not to adversely affect the critical draw ratio since its effects could be compensated for by increasing the strength of external heating. The present work extends prior work in this area by exploring a considerably larger region of parameter space and investigating the practically important issue of draw ratio enhancement. Simple order-of-magnitude estimates based on the results obtained suggest that melt spinning should be able to produce nanaofibers of materials having a step-like variation of viscosity with temperature. The approach and findings of this study may be helpful in guiding experiments in this area.

Acknowledgments

B.S. thanks the Graduate School, University of Minnesota, for providing financial support through the Doctoral Dissertation Fellowship program.

Literature Cited

1. Grafe T, Graham K. Polymeric nanofibers and nanofiber webs: a new class of nonwovens. *Int Nonwovens J*. 2003;12:51–55.
2. Huang ZM, Zhang YZ, Kotaki M, Ramakrishna S. A review on polymer nanofibers by electrospinning and their applications in nanocomposites. *Compos Sci Technol*. 2003;63:2223–2253.

3. Jayaraman K, Kotaki M, Zhang Y, Mo X, Ramakrishna S. Recent advances in polymer nanofibers. *J Nanosci Nanotechnol*. 2004;4:52–65.
4. Zhang Y, Lim CT, Ramakrishna S, Huang ZM. Recent development of polymer nanofibers for biomedical and biotechnological applications. *J Mater Sci Mater Med*. 2005;16:933–946.
5. Burger C, Hsiao BS, Chu B. Nanofibrous materials and their applications. *Annu Rev Mater Res*. 2006;36:333–368.
6. Blyler LL, Gieniewski C. Melt spinning and draw resonance studies on a poly(α-methylstyrene/silicone) block compound. *Polym Eng Sci*. 1980;20:140–148.
7. Wylie JJ, Huang H, Miura RM. Thermal instability in drawing viscous threads. *J Fluid Mech*. 2007;570:1–16.
8. Pearson JRA. *Mechanics of Polymer Processing*. New York: Elsevier Applied Science, 1985.
9. Denn MM. Continuous drawing of liquids to form fibers. *Annu Rev Fluid Mech*. 1980;12:365–387.
10. Jung HW, Jae HS, Hyun JC. Analysis of the stablizing effect of spinline cooling in melt spinning. *J Non-Newtonian Fluid Mech*. 1999;87:165–174.
11. Huang H, Miura RM, Ireland W, Puil E. Heat-induced stretching of a glass tube under tension: application to glass microelectrodes. *SIAM J Appl Math*. 2003;63:1499–1599.
12. Howell PD, Wylie JJ, Huang H, Miura RM. Stretching of heated threads with temperature-dependent viscosity: asymptotic analysis. *Discrete Contin Dyn-B*. 2007;7:553–572.
13. Reneker DH, Chun I. Nanometre diameter fibres of polymer, produced by electrospinning. *Nanotechnology*. 1996;7:216–223.
14. Frenot A, Chronakis IS. Polymer nanofibers assembled by electrospinning. *Curr Opin Colloid Interface Sci*. 2003;8:64–75.
15. Ramakrishna S, Fujihara K, Teo WE, Lim TC, Ma Z. *An Introduction to Electrospinning and Nanofibers*. Singapore: World Scientific Publishing, 2005.
16. Ellison CJ, Phatak A, Giles DW, Macosko CW, Bates FS. Melt blown nanofibers: fiber diameter distributions and onset of fiber breakup. *Polymer*. 2007;48:3306–3316.
17. Kwon IK, Kidoaki S, Matsud T. Electrospun nano- to microfiber fabrics made of biodegradable copolyesters: structural characteristics, mechanical properties and cell adhesion potential. *Biomaterials*. 2005;26:3929–3929.
18. Ziabicki K. *Fundamentals of Fiber Formation*. New York: Wiley, 1976.
19. Ziabicki K. *High Speed Fiber Spinning*. New York: Wiley, 1985.
20. Eggers J. Nonlinear dynamics and breakup of free-surface flows. *Rev Mod Phys*. 1997;69:865–929.
21. Sauter US, Buggisch HW. Stability of initially slow viscous jets driven by gravity. *J Fluid Mech*. 2005;533:237–257.
22. Shah YT, Pearson JRA. On the stability on nonisothermal fiber spinning—general case. *Ind Eng Chem Fundam*. 1972;11:150–153.
23. Fisher RJ, Denn MM. Mechanics of nonisothermal polymer melt spinning. *AIChE J*. 1977;23:23–28.
24. Whitehead JA, Helfrich KR. Instability of flow with temperature-dependent viscosity: a model of magma dynamics. *J Geophys*. 1991; 96(B3):4145–4155.
25. Hyun JC. Theory of draw resonance, part I: newtonian fluids. *AIChE J*. 1978;24:418–422.
26. Hyun JC. Theory of draw resonance, part II: power-law and Maxwell fluids. *AIChE J*. 1978;24:423–426.
27. Larson RG. Instabilities in viscoelastic flows. *Rheol Acta*. 1992;31: 213–263.
28. Kim BM, Hyun JC, Oh JS, Lee SJ. Kinematic waves in the isothermal melt spinning of Newtonian fluids. *AIChE J*. 1996;42:3164–3169.
29. Pearson JRA, Shah YT. Stability analysis of the fiber spinning process. *J Rheol*. 1972;16:519–533.
30. Hagen T. On the effects of spinline cooling and surface tension in fiber spinning. *Z Angew Math Mech*. 2002;82:545–558.
31. Hagen T, Langwallner B. A numerical study on the suppression of draw resonance by inertia. *Z Angew Math Mech*. 2006;86:63–70.
32. German R, Khayat RE, Cui JK. Influence of inertia and gravity on the stability of filament jet flow. *Phys Fluids*. 2006;18:064108–1–16.
33. Kargupta K, Konnur R, Sharma A. Instability and pattern formation in thin liquid films on chemically heterogeneous substrates. *Langmuir*. 2000;16:10243–10253.
34. Zope M, Kargupta K, Sharma A. Self-organized structures in thin liquid films on chemically heterogeneous substrates: effect of antagonistic short and long range interactions. *J Chem Phys*. 2001;114: 7211–7221.

Manuscript received Dec. 27, 2007, revision received July 2, 2008, and final revision received Sept. 18, 2008.